Supporting Information

Room-Temperature Flexible Quasi-Solid-State Rechargeable Na–O_2 Batteries

*Jiaqi Wang, Youxuan Ni, Junxiang Liu, Yong Lu, Kai Zhang, Zhiqiang Niu and Jun Chen**

Key Laboratory of Advanced Energy Materials Chemistry (Ministry of Education), Renewable Energy Conversion and Storage Center, College of Chemistry (RECAST), Nankai University, Tianjin 300071, China

*Correspondence: chenabc@nankai.edu.cn

Table of Contents

Figure S1. Atomic force microscopy image with 2D and 3D view of QPE····· S4

Figure S2. Cross-section analysis of the height and surface roughness (Rq or average deviation) of QPE····· ·····S5

Figure S3. Inflammability of Celgard separator before loading with liquid electrolyte· ····· S6

Figure S4. The stress-strain curve of QPE····· ···· ·····S7

Figure S5. Thermal gravity analysis of QPE, Celgard separator and glass fiber separator ·····S8

Figure S6. Electrolyte leakage of Na–O_2 batteries ····· ·····S9

Figure S7. TEM image and SAED of the commercial fumed silica in hydrophobic··· ··S10

Figure S8. Raman of SiO_2, PVdf-HFP and polymer matrix of QPE·· · ·S11

Figure S9. Nyquist plots of the impedance spectra of the dried QPE·· · ·S12

Figure S10. Electrostatic potential (ESP) map of the PVdF-HFP chain····· ·····S13

Figure S11. Pathway of Na^+ ions migration along the PVDF chain···· ····S14

Figure S12. Top view of charge transfer after the adsorption of Na^+ ions··· ····S15

Figure S13. Charge redistribution after the adsorption of Na^+ ions···· ·· ·S16

Figure S14. The pore size distribution of QPE···· ···S17

Figure S15. Electrolyte penetration with Celgard separator and QPE····· S18

Figure S16. Voltage profiles of Na-Na symmetric cells with Celgard separator or QPE·· ····S19

Figure S17. The CV curves of quasi-solid-state Na–O_2 battery in argon atmosphere S20

Figure S18. Voltage profiles of Na–O_2 battery with glass fiber separator with a cut-off capacity of 1000 mAh g^{-1} S21

Figure S19. Voltage profiles of Na–O_2 battery with Celgard separator with cut-off capacity of 1000 mAh g^{-1}· ·S22

Figure S20. The median discharge/charge voltage gap at various current densities····· ·· ··S23

Figure S21. Discharge profiles of Na–O_2 batteries with carbon paper and carbon paper + Super P ···· ·S24

Figure S22. Discharge profiles of Na–O_2 batteries with carbon cloth and carbon cloth + Super P S25

Figure S23. Contact angle measurement of QPE thin film towards water··· ··S26

Figure S24. The optical images of Na metal covered with Celgard separator/QPE after placed in O_2 and air atmosphere for 30 minutes. ··· ··S27

Figure S25. Raman of Na metal separated by Celgard separator/QPE from oxygen and air atmosphere, respectively. ··S28

Figure S26. Photograph of aluminum foil on a film applicator and polymer solution on the aluminum foil····· ·S29

Figure S27. Photographs of Na foil anode, QPE, carbon paper and Super P/carbon paper·· ·S30

Figure S28. The voltage profile of pouch-type Na–O_2 battery with QPE····· ···S31

Figure S29. Photograph of the assembled pouch-type Na–O_2 batter**y**··· ··S32

Figure S30. The morphology evolution of the air cathode···· ·····S33

Figure S31. XRD patterns of pristine, discharged and recharged air cathodes·· ··S34

Figure S32. Raman spectra of pristine, discharged and recharged air cathodes· ····S35

Figure S33. Photograph of bendable carbon cloth after spraying Super P carbon···· ··S36

Figure S34. Fatigue test of flexible QPE-based Na–O_2 batter**y** ····· ····S37

Figure S35. Voltage profiles for flexible QPE-based Na–O_2 batter**y**····· ····S38

Table S1. Comparisons of the electrochemical performance of liquid-based Na–O_2 batteries in recent works and all non-liquid-based Na–O_2 batteries····· ···S39

References·····S40

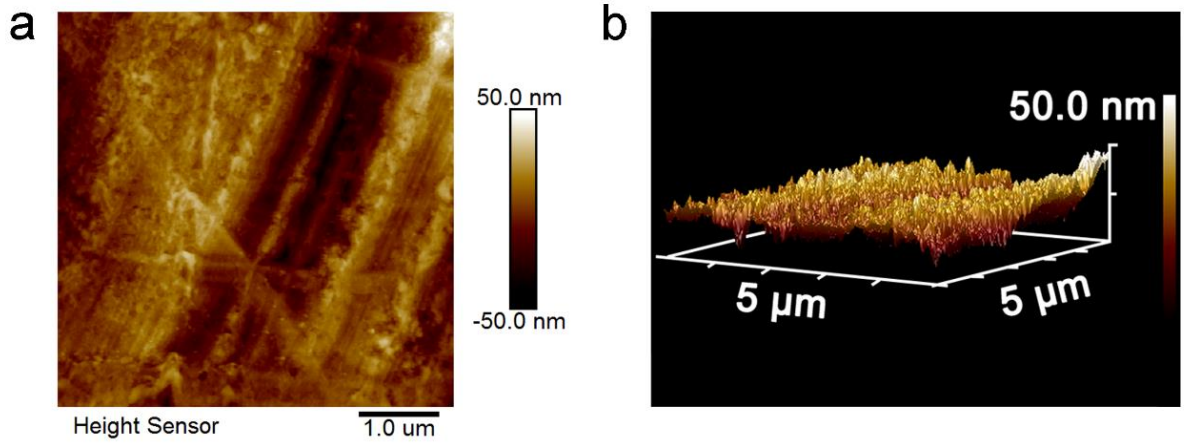

Figure S1. Atomic force microscopy image with (a) 2D and (b) 3D view of QPE.

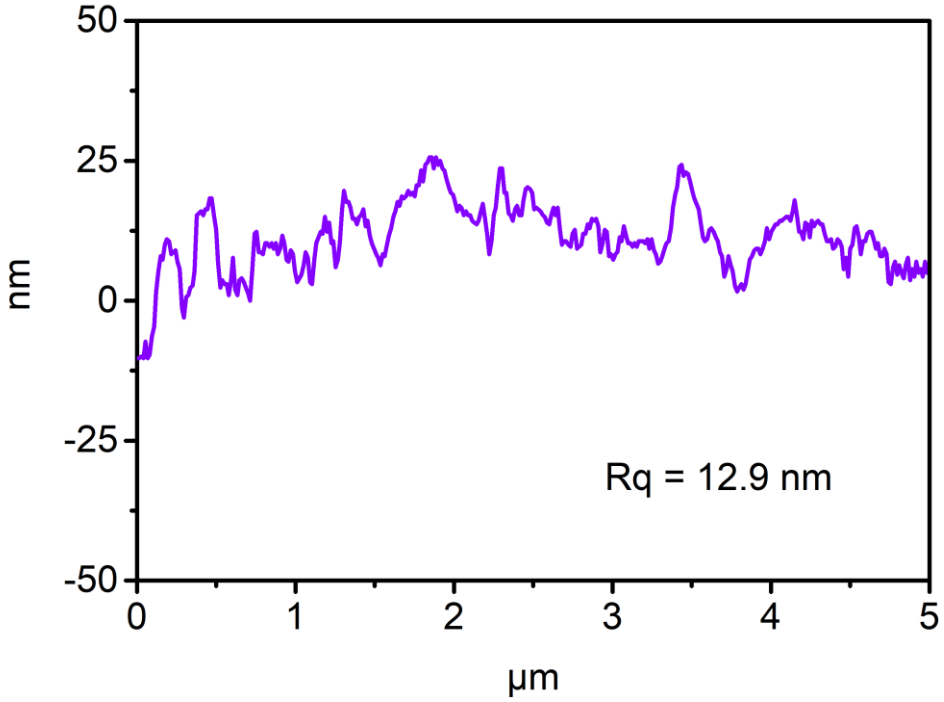

Figure S2. Cross-section analysis of the height and surface roughness (Rq or average deviation) of QPE.

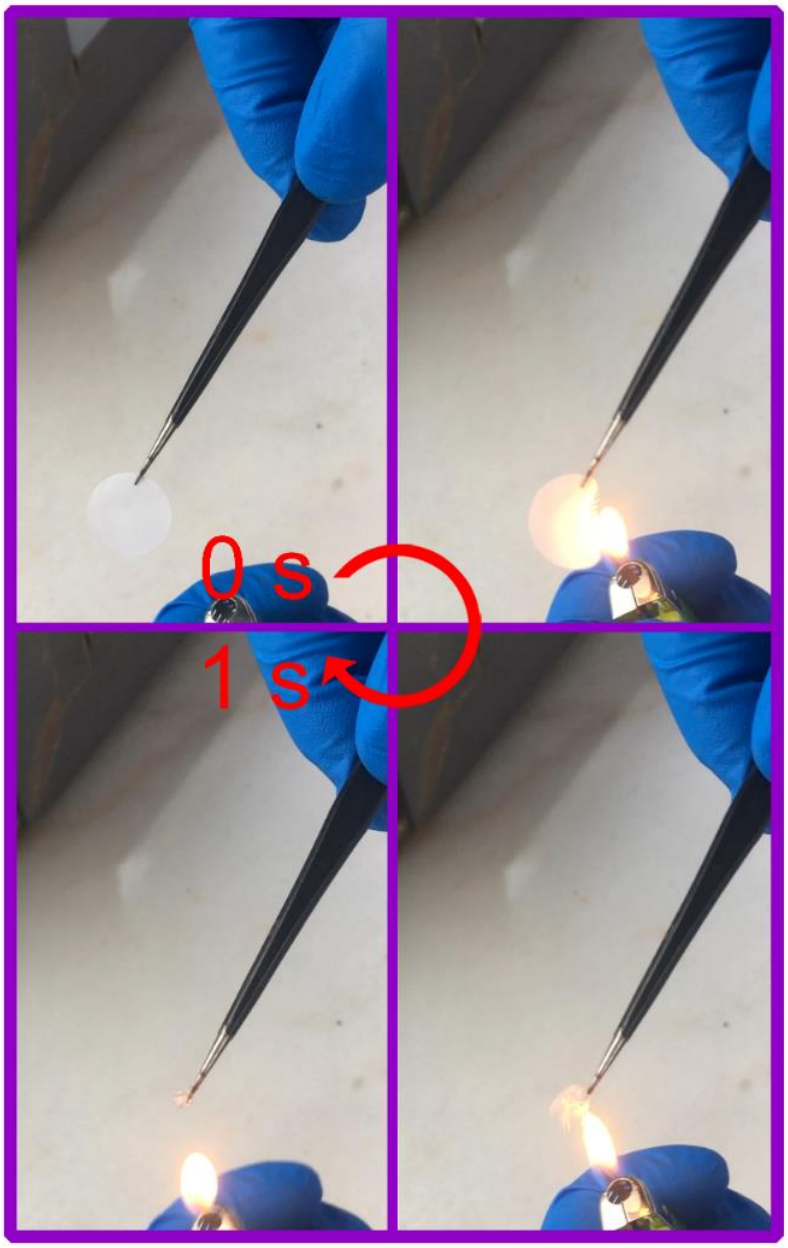

Figure S3. Inflammability of Celgard separator before loading with liquid electrolyte.

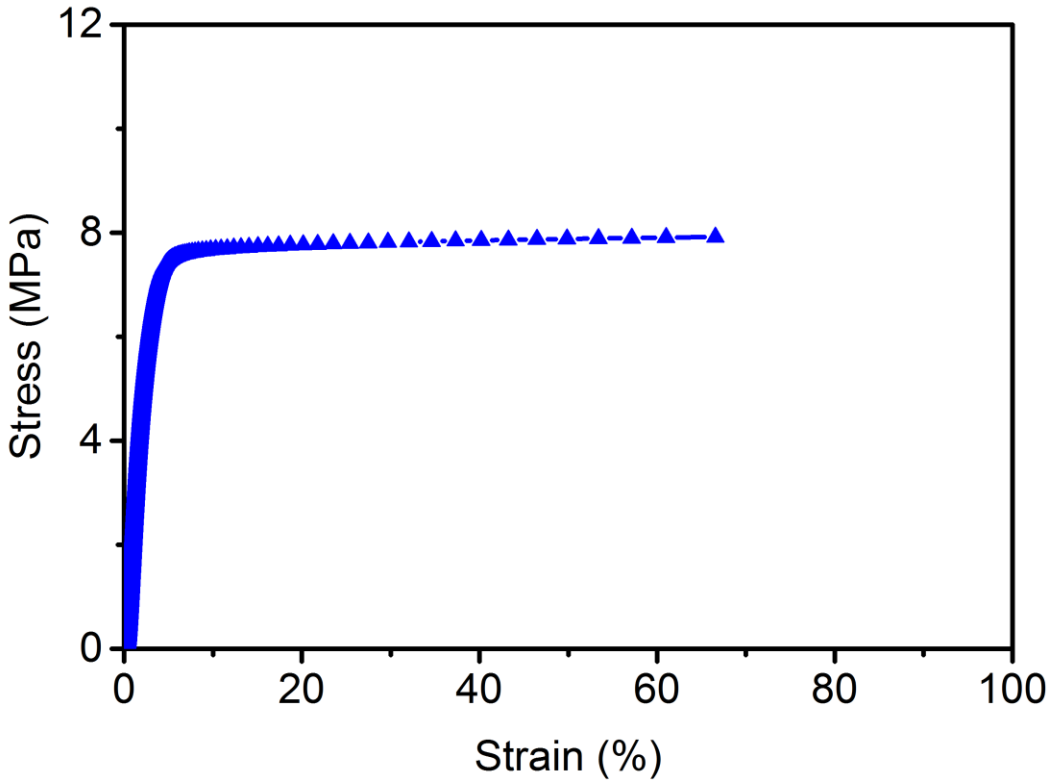

Figure S4. The stress-strain curve of QPE.

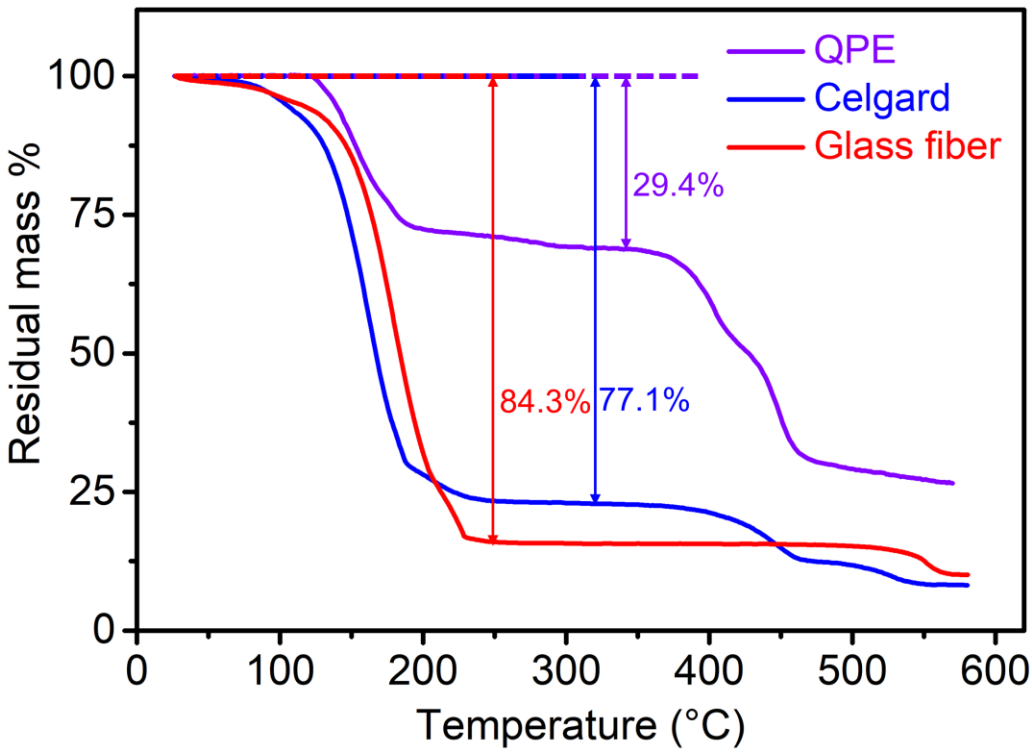

Figure S5. Thermogravimetric analysis of QPE, Celgard separator and glass fiber separator. The content of TEGDME is 29.4 wt%, 77.1 wt% and 84.3 wt%, respectively.

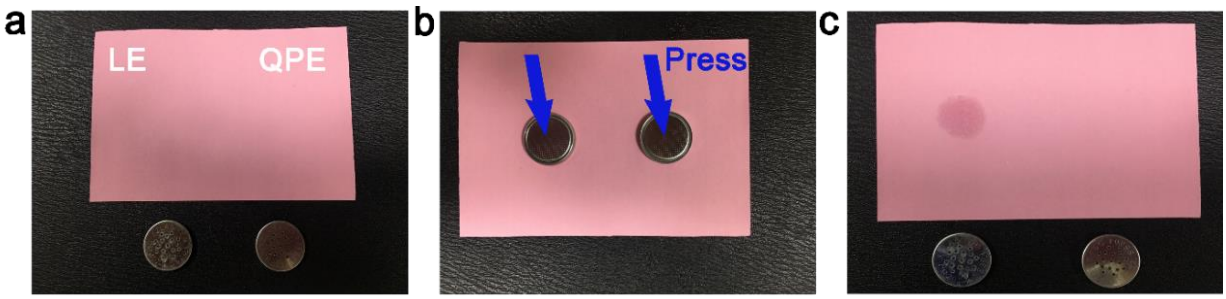

Figure S6. Electrolyte leakage of $Na–O_2$ batteries. $Na–O_2$ batteries with (a) LE and QPE. (b) Before and (c) after pressing $Na–O_2$ batteries on a piece of dry paper.

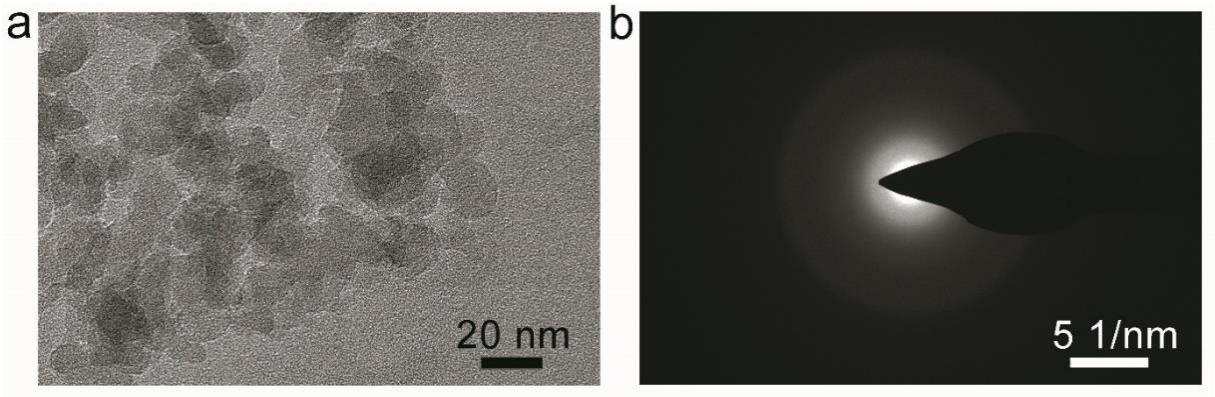

Figure S7. (a) TEM image of the commercial hydrophobic fumed silica. (b) SAED of SiO_2.

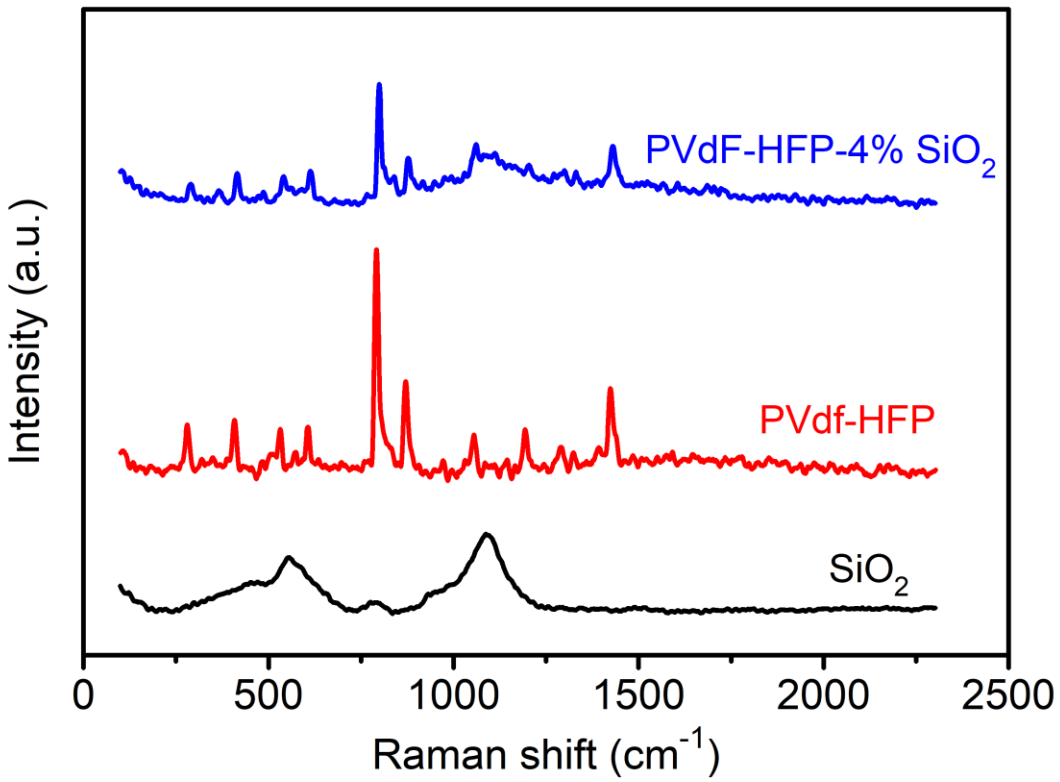

Figure S8. Raman of SiO_2, PVdf-HFP and polymer matrix of QPE.

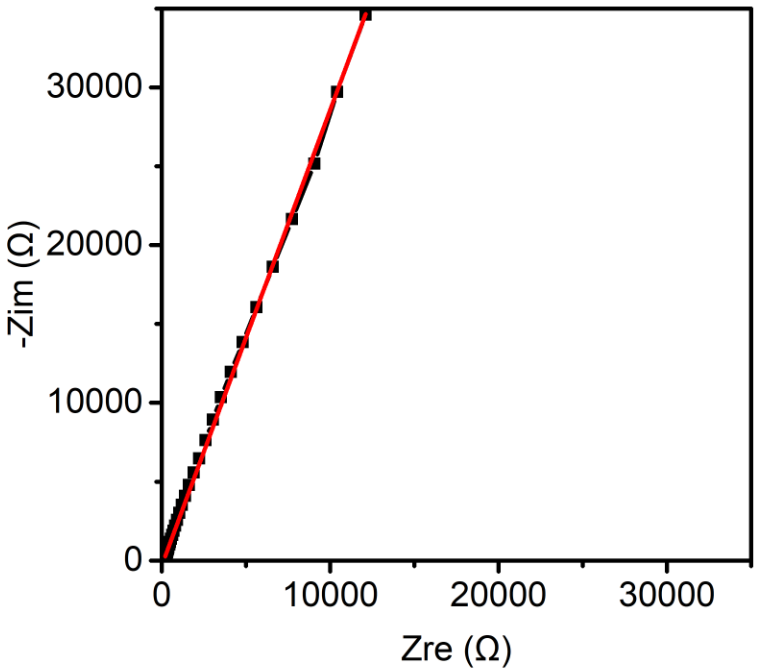

Figure S9. Nyquist plots of the impedance spectra.

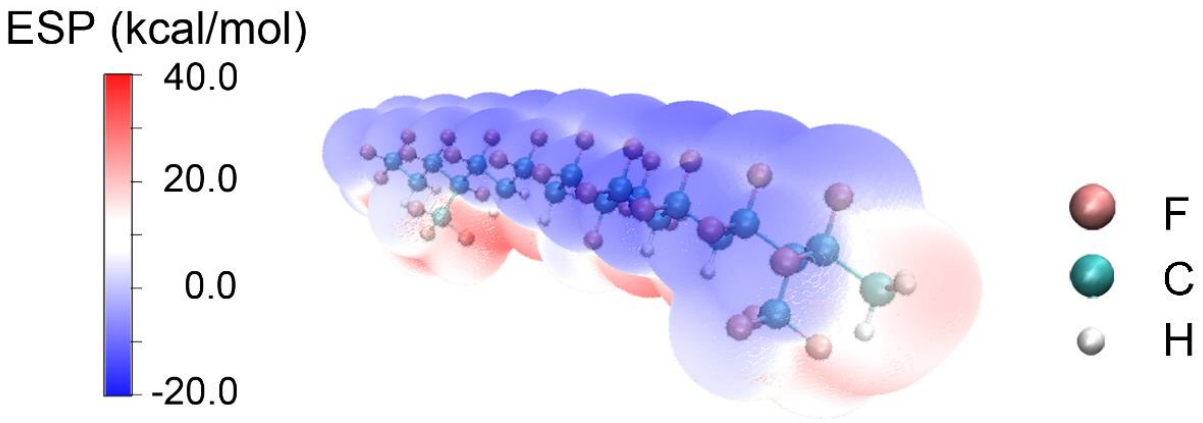

Figure S10. Electrostatic potential (ESP) map of the PVdF-HFP chain.

The electrostatic potential (ESP) map was calculated on the basis of the PVdF-HFP segment. The structure of the segment was obtained from Gaussian 16 with the B3LYP functional[1-3] and 6-31+G*[4-6] basis set. Then, the ESP map is plotted on the van der Waals surface (the value of electric density isosurface is 0.001 a.u.) of the segment by using the quantitative analysis of molecular surface in the open source Multiwfn package. The most favorable adsorption sites for Na^+ are usually located at the site with the most negative electrostatic potential. For ion migration, the migration pathway is commonly associated with the valley of the electrostatic potential surface, where the ion will experience smallest energy fluctuation during migration from the most favorable adsorption site to another.

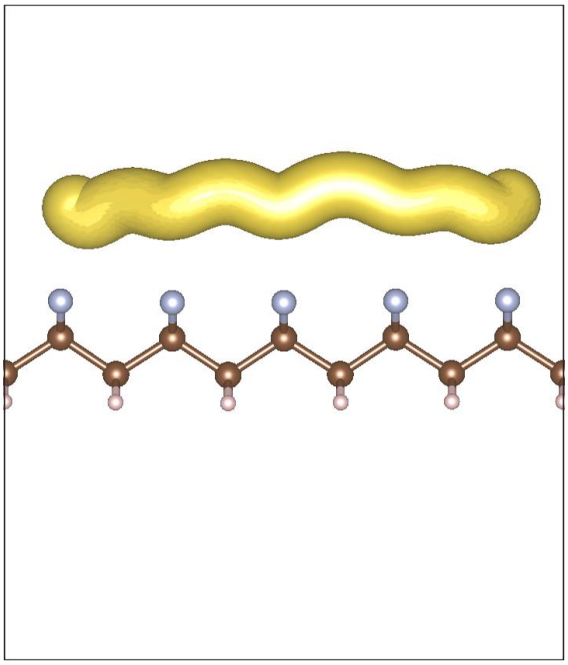

Figure S11. Pathway of Na^+ ions migration along the PVDF chain. The yellow strip indicates the trace of Na^+ ions movements during AIMD simulation.

In order to confirm the results from the climbing image nudged elastic band (CI-NEB) calculation, the ab initio molecular dynamics (AIMD) simulation was carried on the transmission routes of Na^+ ions. The model, same as the one for CI-NEB calculation, was put into a NVT ensemble with a fixed time step of 1 fs. The trace of Na^+ ions movements in 1 ps reveals the transfer of Na^+ ions over the F atoms and along the polymer chain.

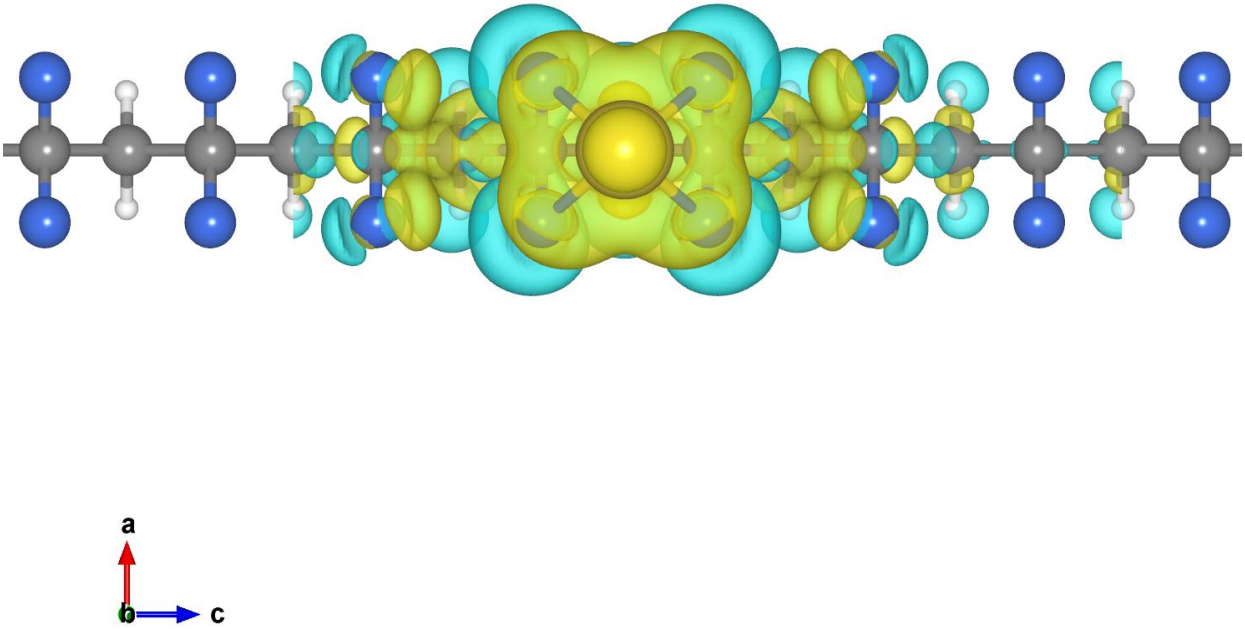

Figure S12. Top view of charge transfer after the adsorption of Na^+ ions. Yellow means electron accumulation and cyan means electron depletion. The yellow, grey, blue and white spheres represent sodium, carbon, oxygen, and hydrogen, respectively.

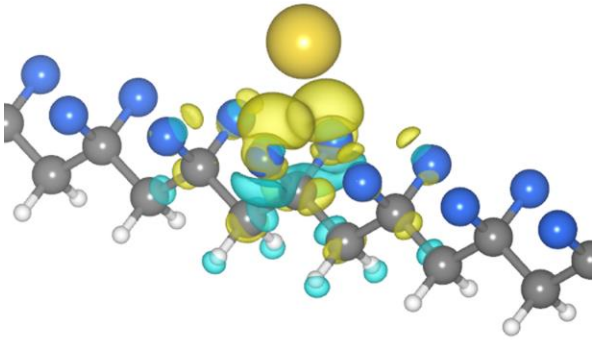

Figure S13. Charge redistribution after the adsorption of Na^+ ions. Yellow means electron accumulation and cyan means electron depletion. The yellow, grey, blue and white spheres represent sodium, carbon, oxygen, and hydrogen, respectively.

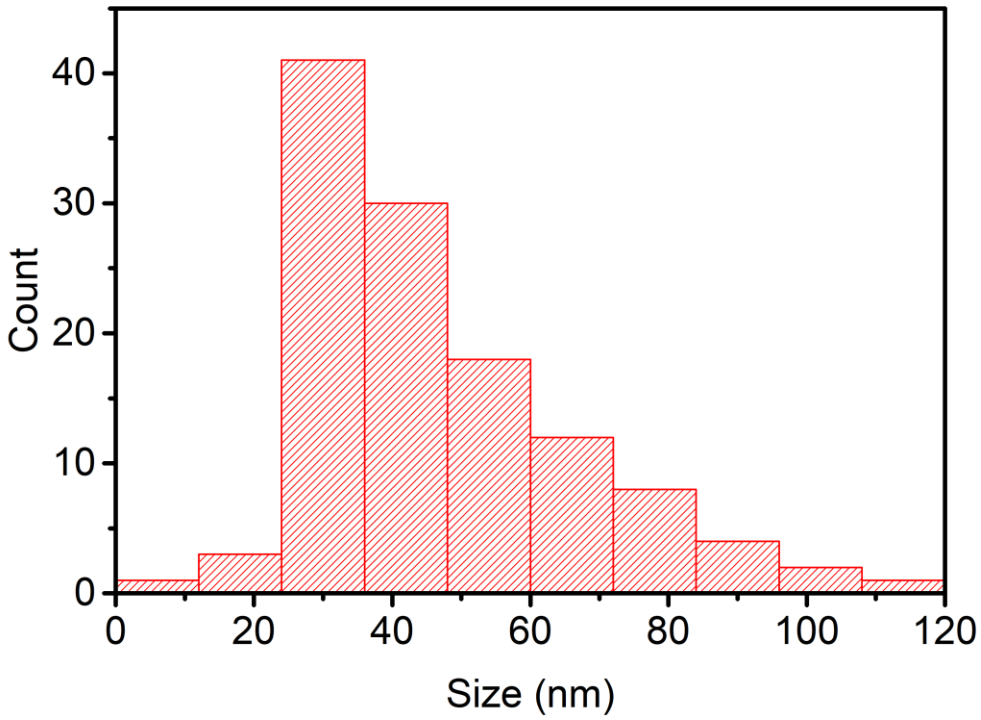

Figure S14. The pore size distribution of QPE. The sampling number is 120. The centered pore size is ~30 nm.

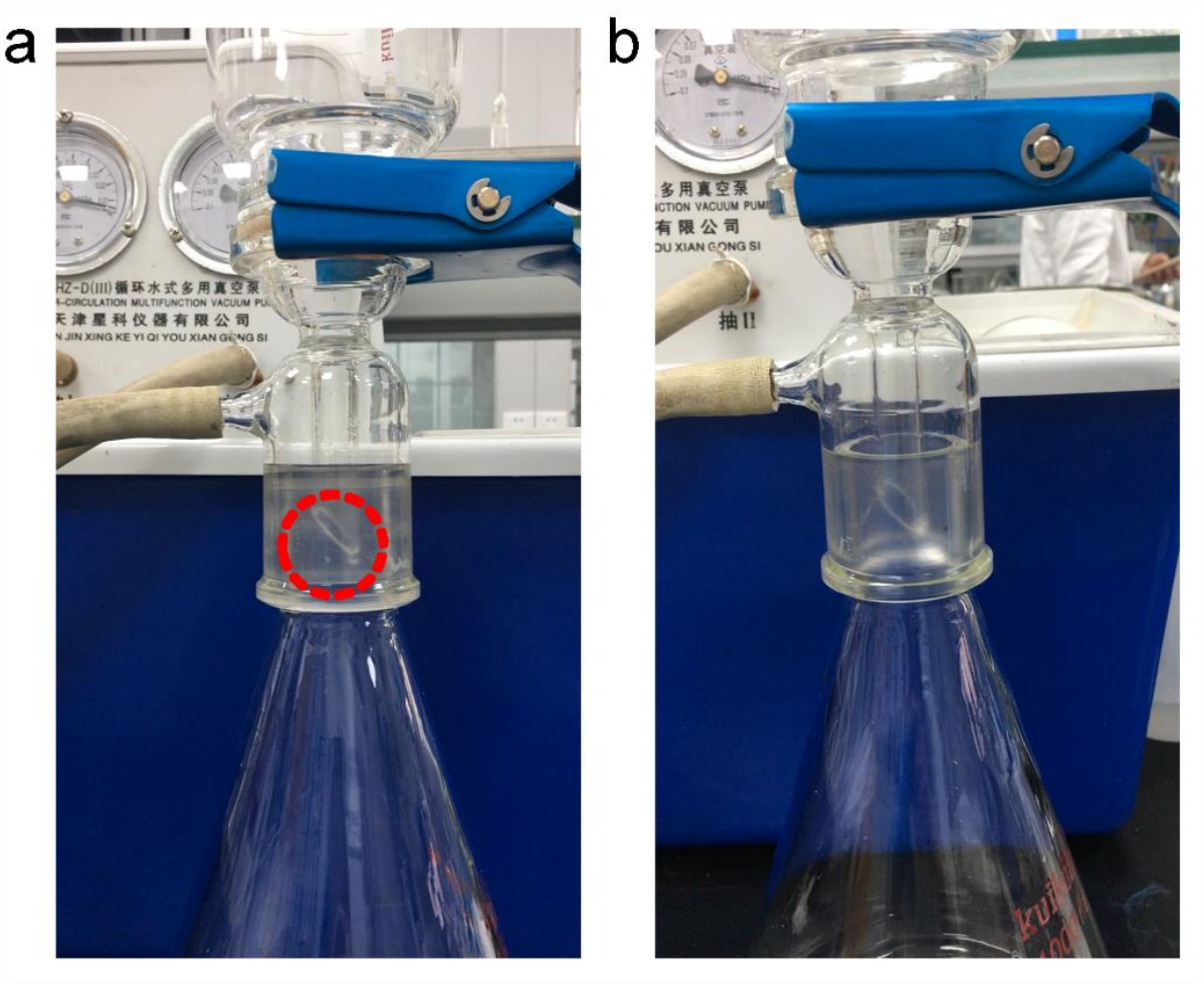

Figure S15. Electrolyte penetration with (a) Celgard separator and (b) QPE.

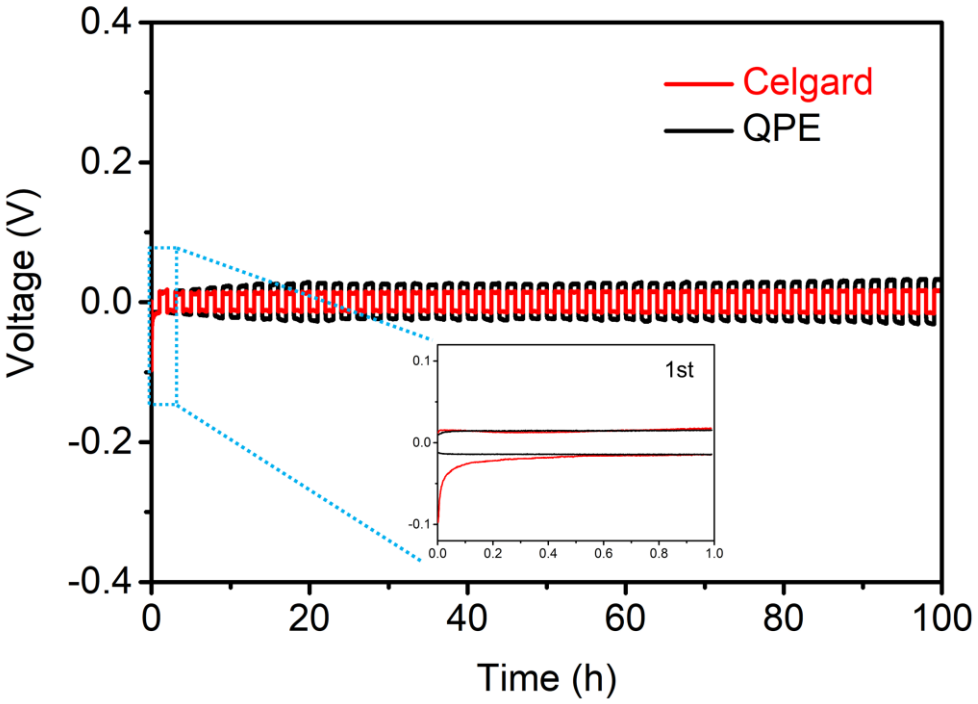

Figure S16. Voltage profiles of Na-Na symmetric cells with Celgard separator or QPE.

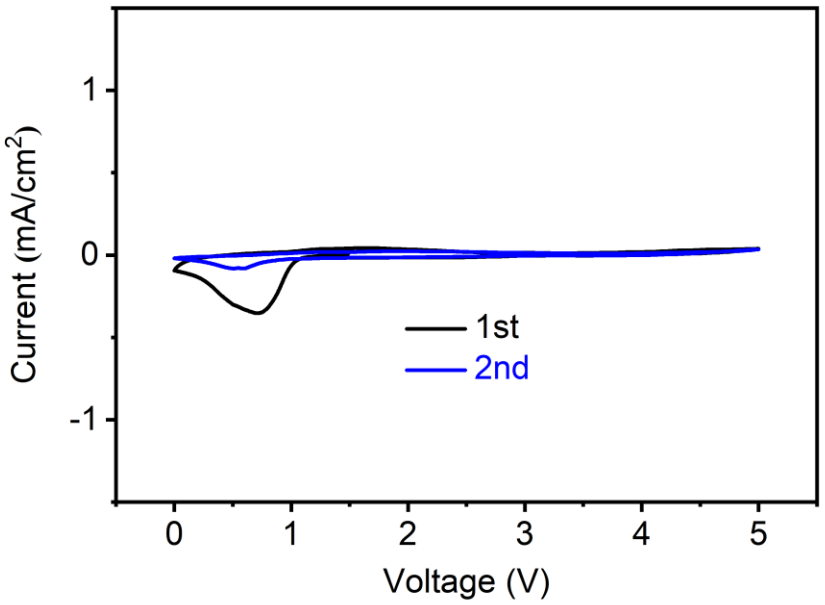

Figure S17. The CV curves of quasi-solid-state $Na–O_2$ battery in argon atmosphere at 0.1 mV s^{-1}.

The CV curves of quasi-solid-state $Na–O_2$ battery in argon atmosphere indicate that the upper and lower limits of batteries' operating voltage are 1.1 and 5.0 V, respectively. The stable window is a potential range versus Na^+/Na, in which the electrolyte will not be oxidized and Na ions will not be inserted into carbon electrode. Quasi-solid-state $Na–O_2$ batteries can operate steadily within this voltage window.

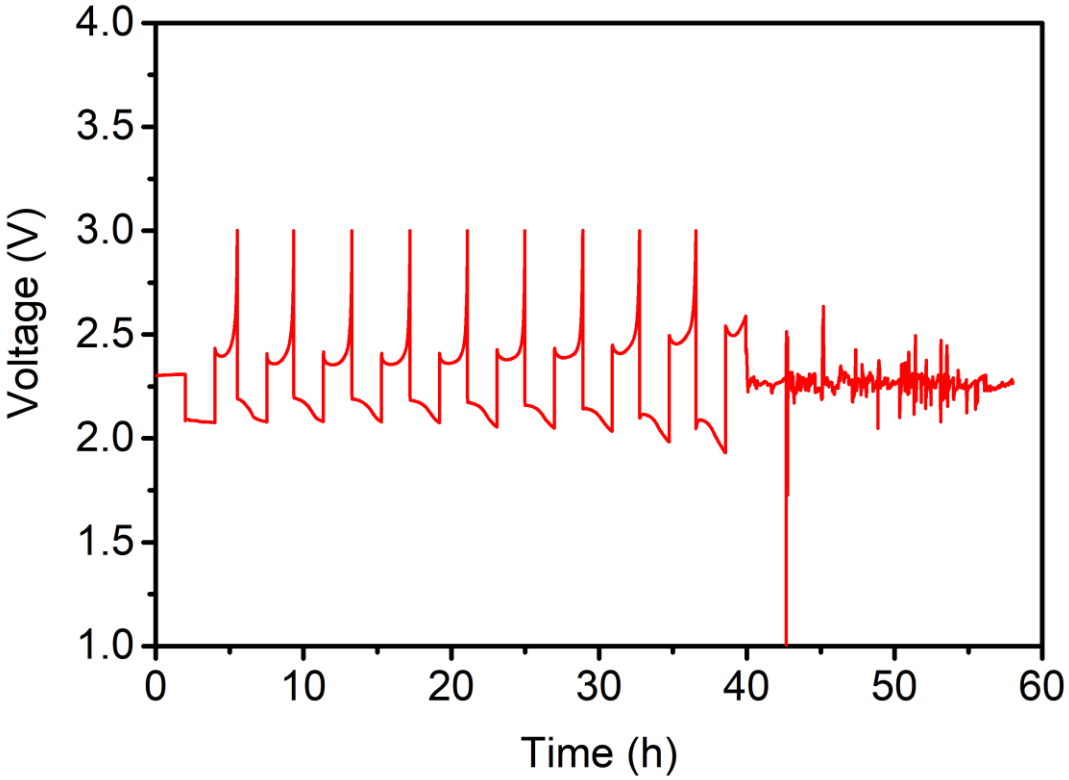

Figure S18. Voltage profiles of Na–O_2 battery with glass fiber separator with a cut-off capacity of 1000 mAh g^{-1}.

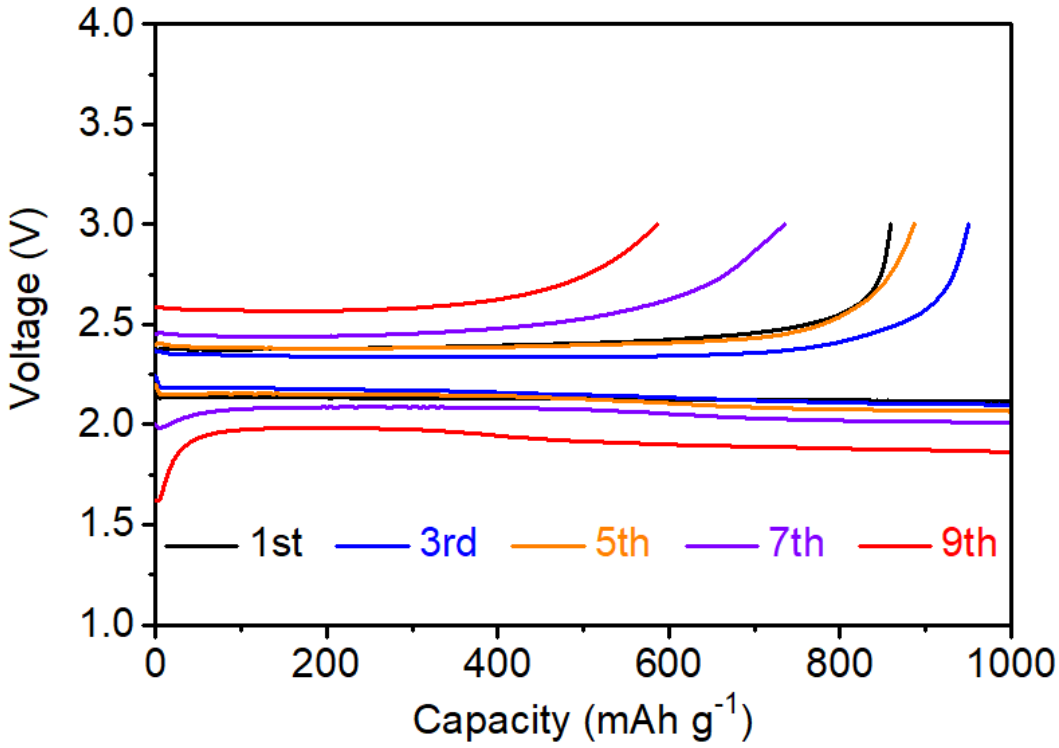

Figure S19. Voltage profiles of Na–O_2 battery with Celgard separator with a cut-off capacity of 1000 mAh g^{-1}.

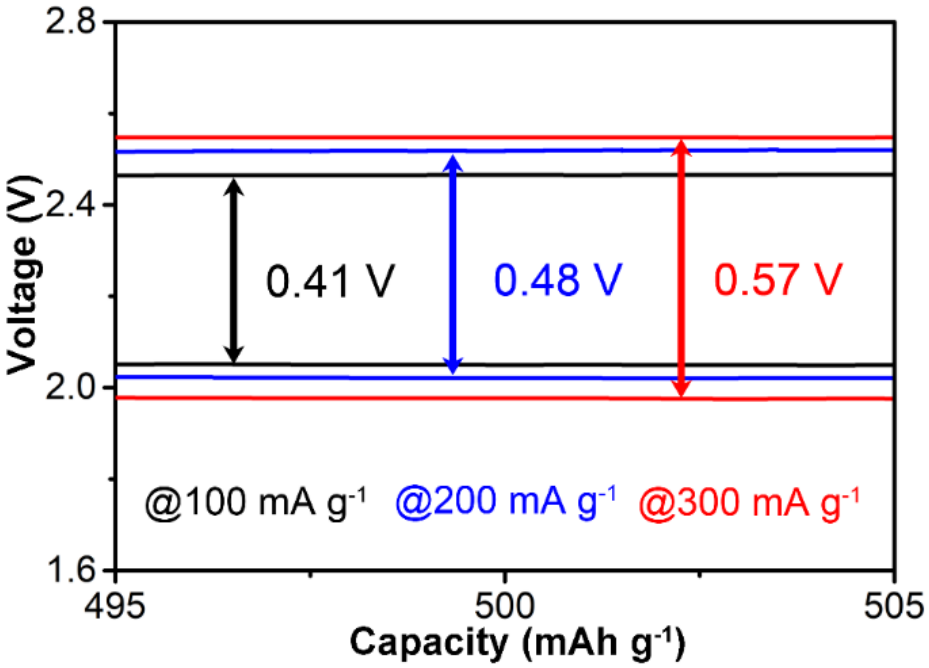

Figure S20. The median discharge/charge voltage gap at various current densities.

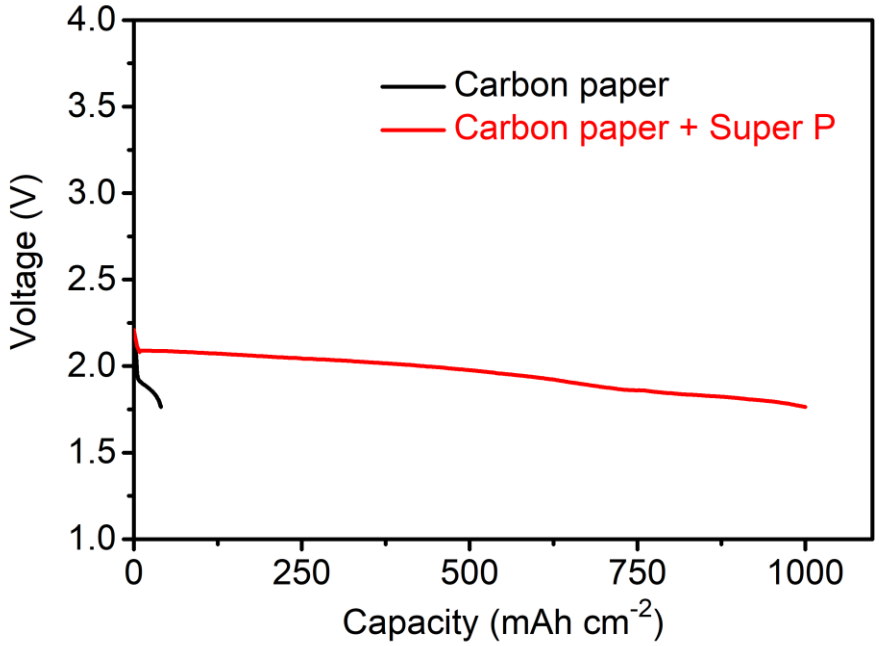

Figure S21. Discharge profiles of $Na–O_2$ batteries with carbon paper and carbon paper + Super P.

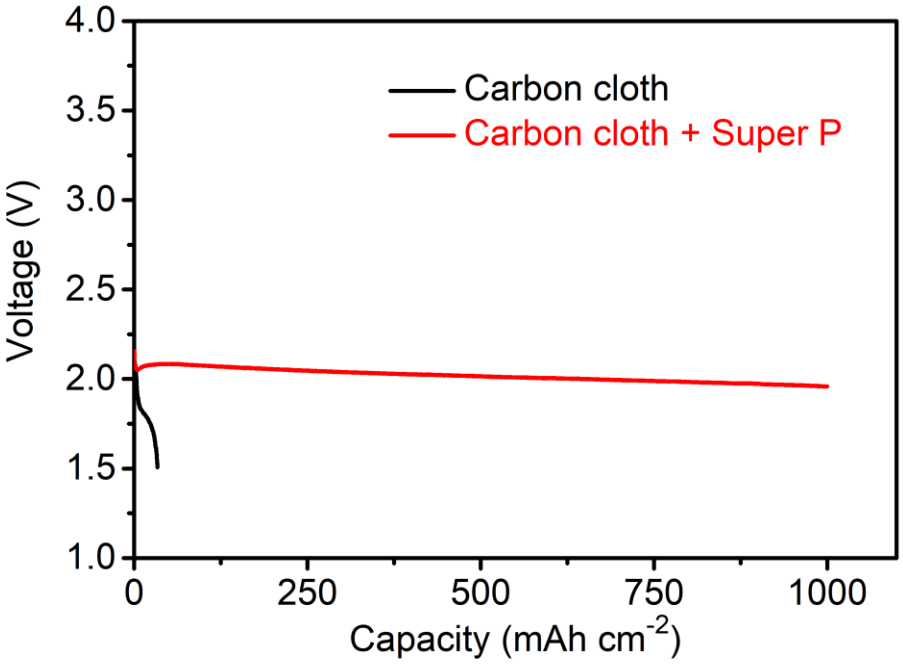

Figure S22. Discharge profiles of Na–O_2 batteries with carbon cloth and carbon cloth + Super P.

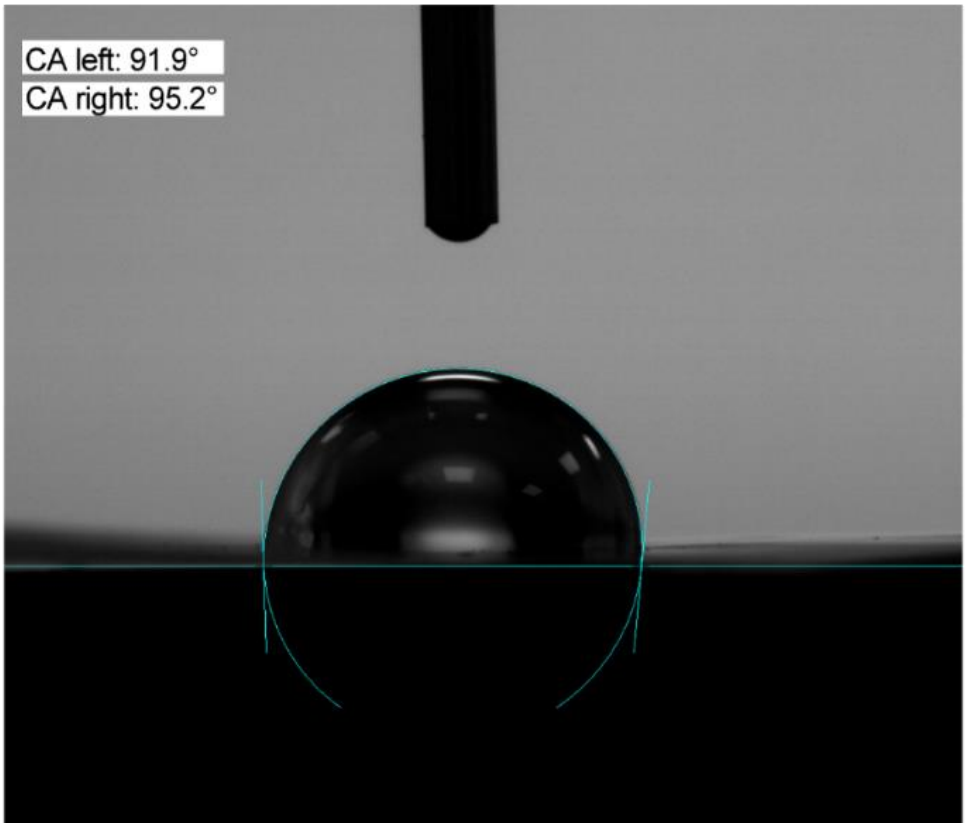

Figure S23. Contact angle measurement of QPE thin film toward water.

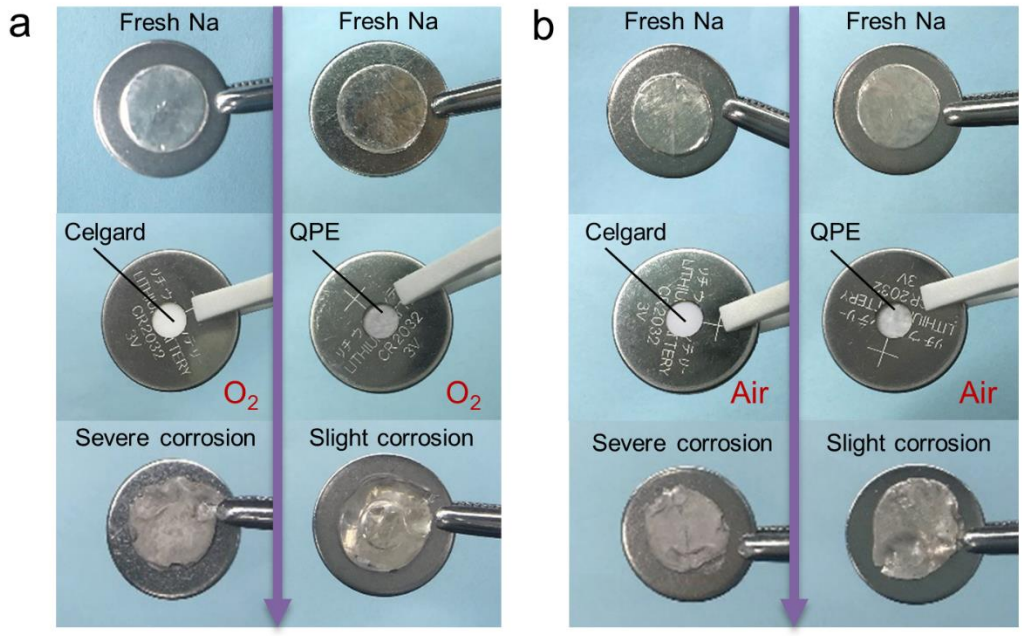

Figure S24. The optical images of Na metal covered with Celgard separator/QPE after placed in (a) O_2 and (b) air atmosphere for 30 minutes.

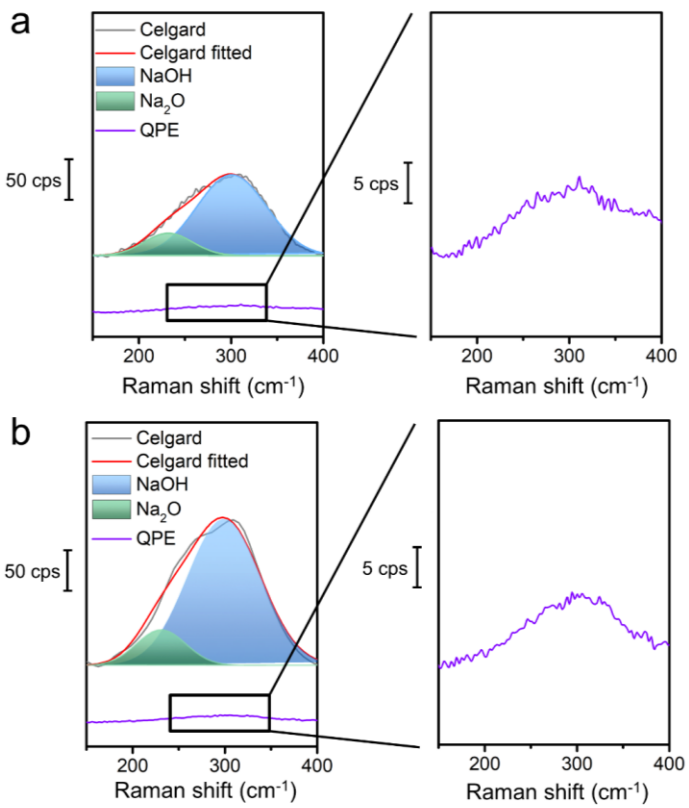

Figure S25. Raman of Na metal separated by Celgard separator/QPE from (a) oxygen and (b) air atmosphere, respectively.

We encapsulated the metal Na in the battery shell with the hole sealed by QPE or Celgard on the cathode side, and placed it in oxygen/air for 30 min. The surface compositions of Na metal were detected by Raman spectroscopy. As shown in Figure S24a, Na metal covered by Celgard separator shows the stronger Raman peaks around 235 cm^{-1} and 300 cm^{-1}, corresponding to Na_2O and NaOH, respectively.[7] On the contrast, the intensity of Raman peaks for Na metal covered by QPE is much weaker (Figure S24b). Additionally, NaOH is observed on the surface of Na metal placed in the oxygen atmosphere. It can be attributed to the trace water, which commonly exists in oxygen and is hard to be removed completely.

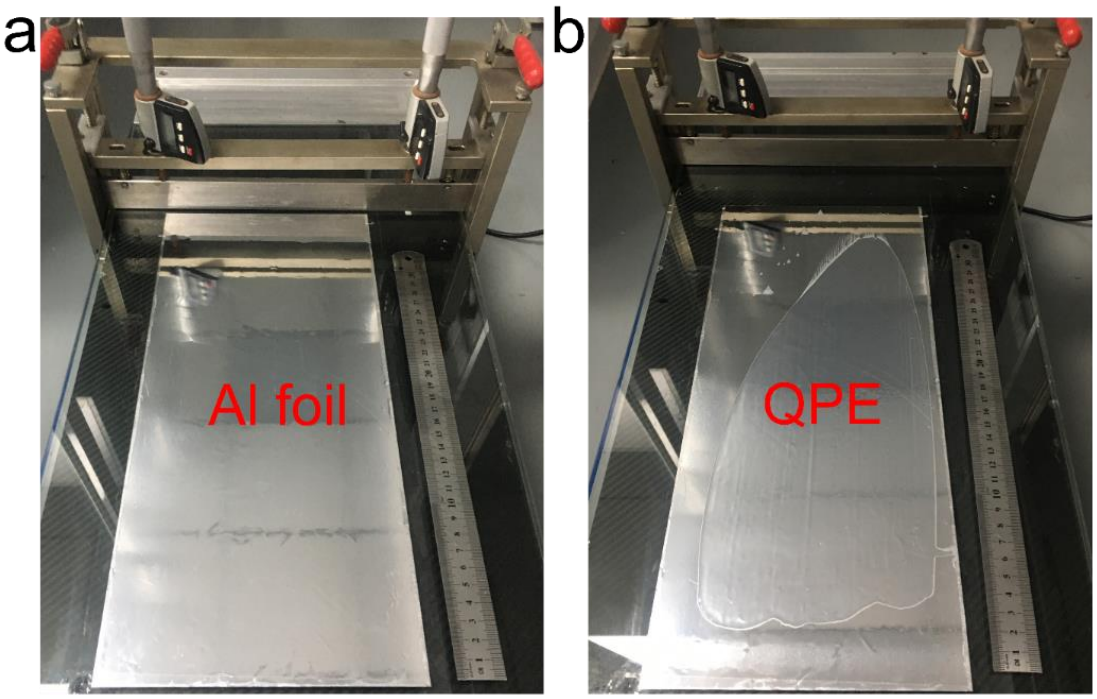

Figure S26. Photograph of (a) aluminum foil on a film applicator and (b) polymer solution on the aluminum foil.

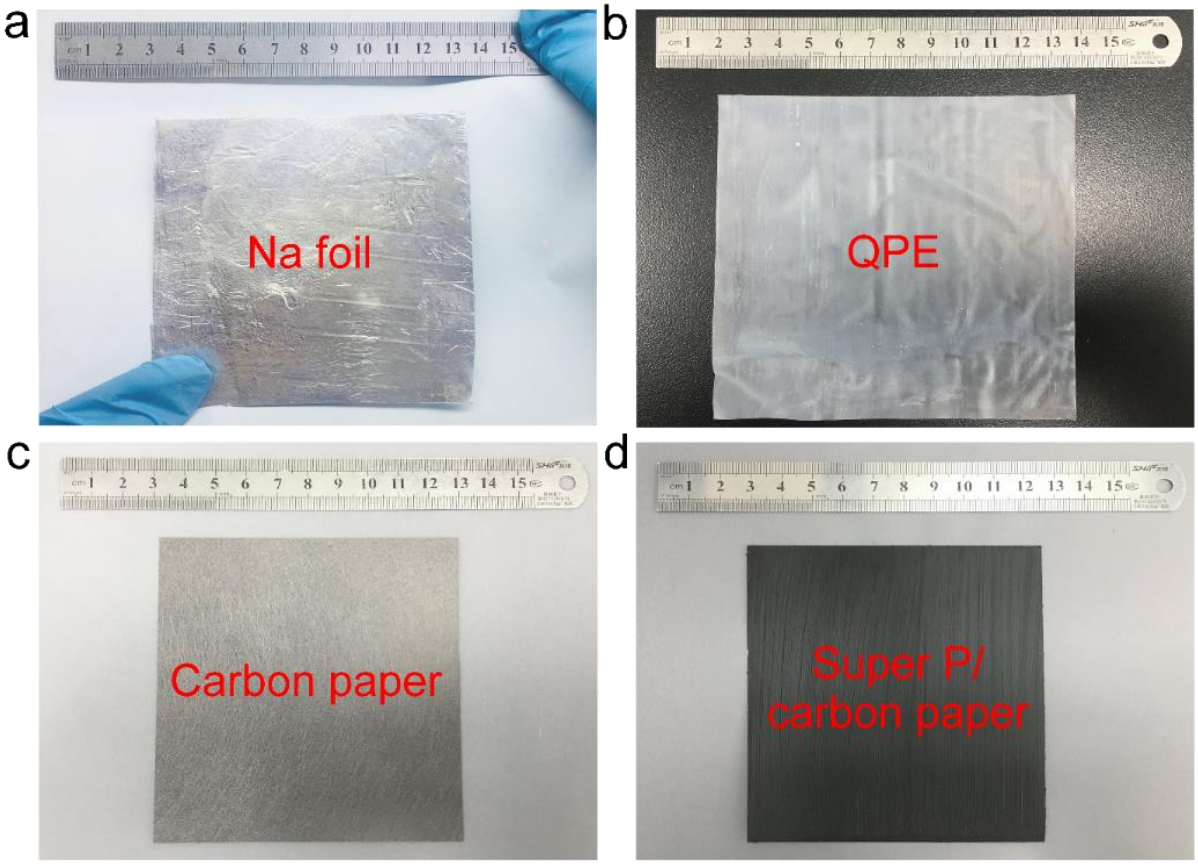

Figure S27. Photographs of (a) Na foil anode, (b) QPE, (c) carbon paper and (d) Super P/carbon paper.

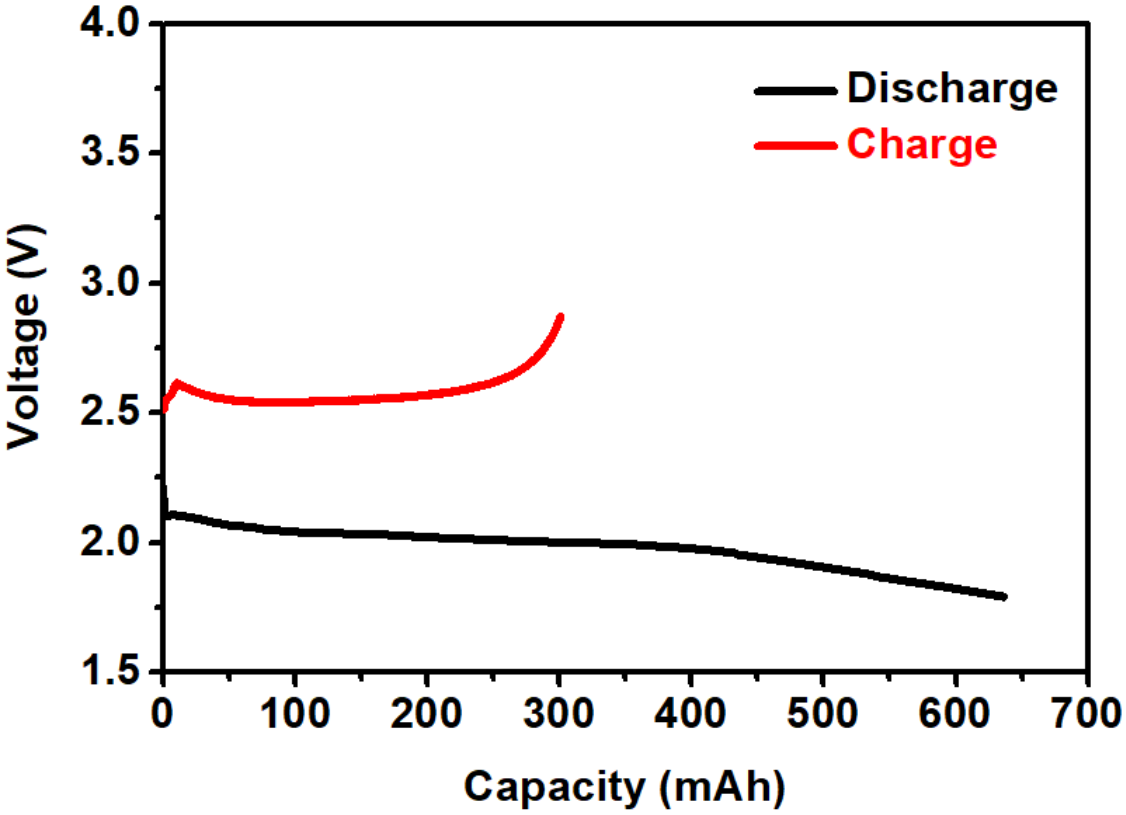

Figure S28. The voltage profile of the large-scale pouch-type Na–O_2 battery with QPE.

Figure S29. Photograph of the assembled large-scale pouch-type $Na–O_2$ battery.

The energy density of the large-scale pouch-type $Na–O_2$ battery is 335 Wh kg^{-1}, which is based on the total mass of the whole battery and obtained by the formula of 636.1 mAh × 2.0 V/3.8 g.

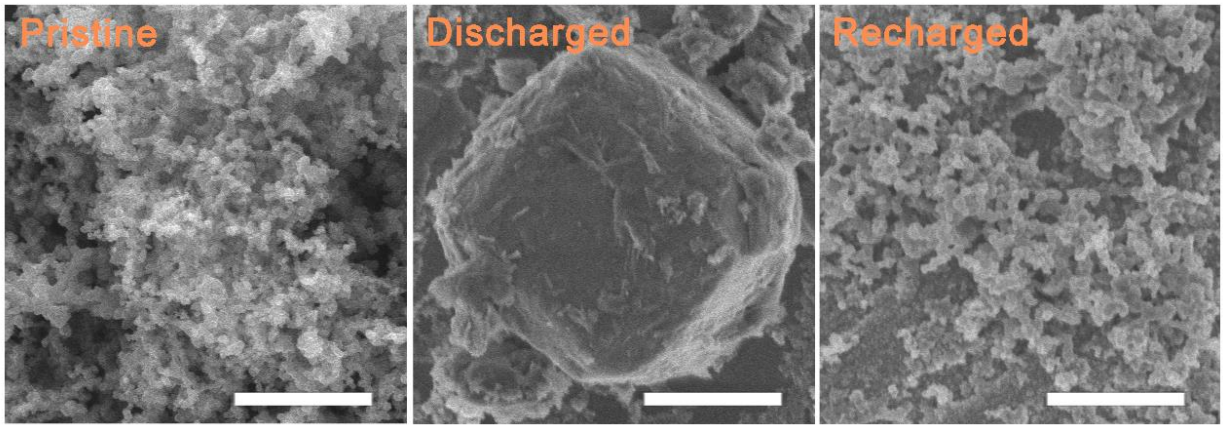

Figure S30. The morphology evolution of the air cathode. The corresponding SEM images of Super P cathode at pristine state, discharge state and recharge state. Scale bar: 1 μm.

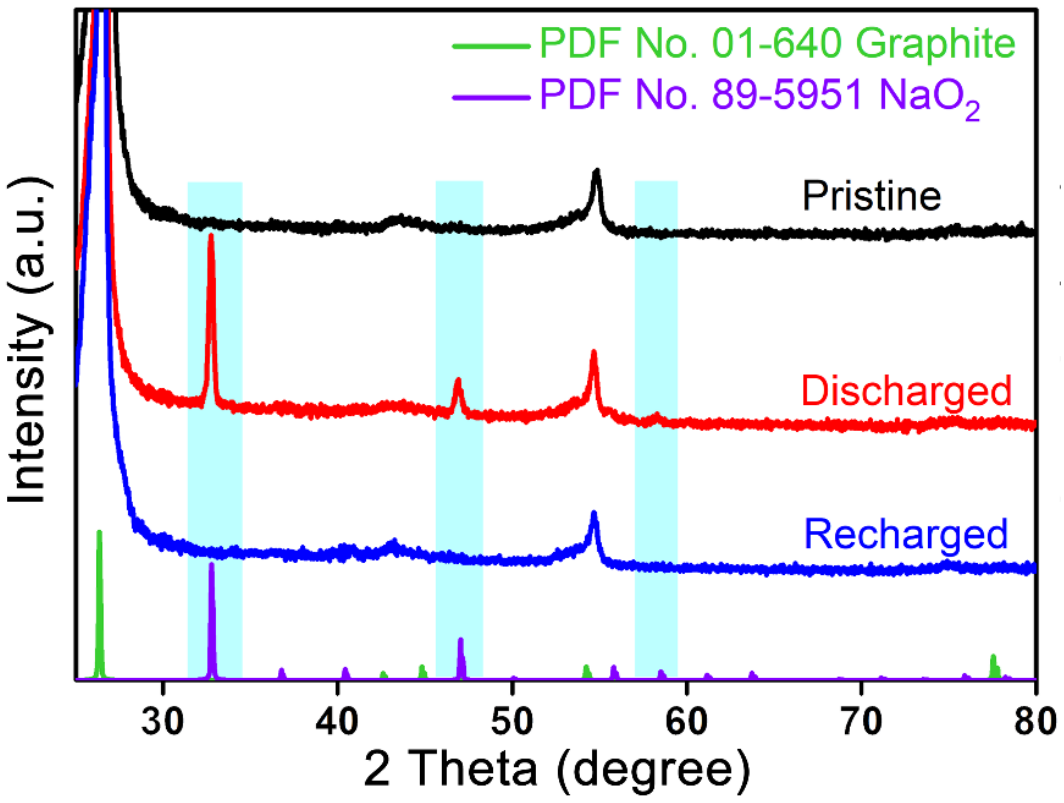

Figure S31. XRD patterns of pristine, discharged and recharged air cathodes.

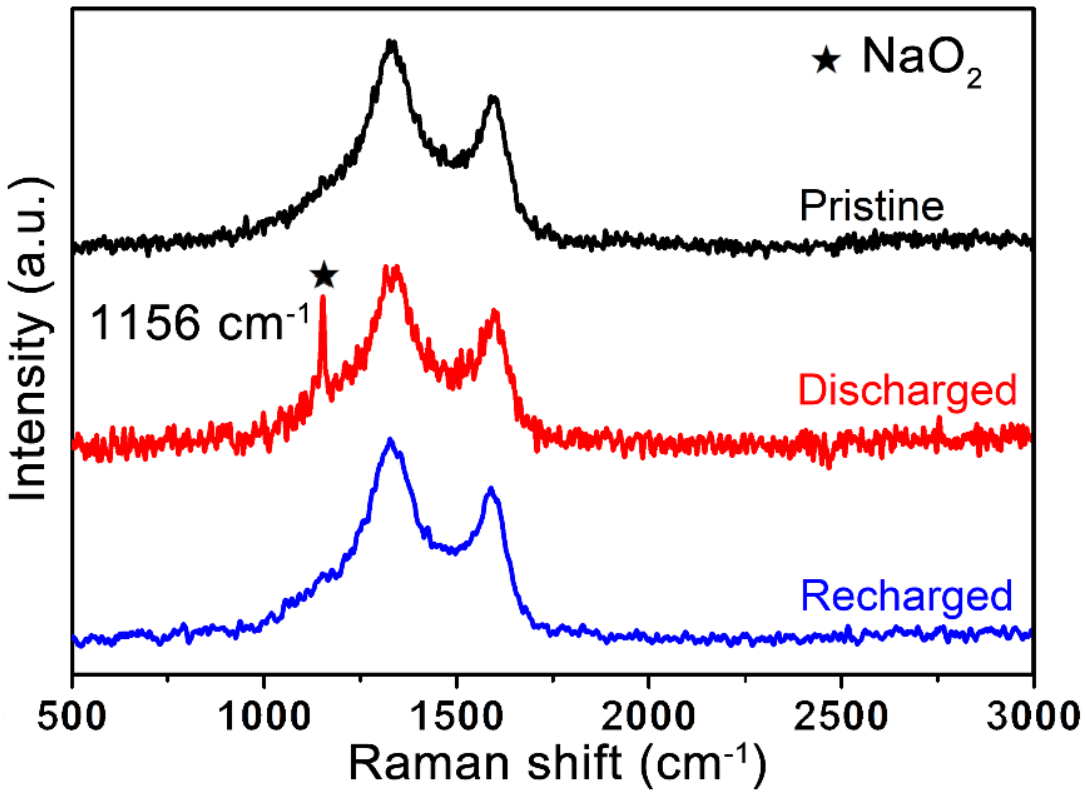

Figure S32. Raman spectra of pristine, discharged and recharged air cathodes.

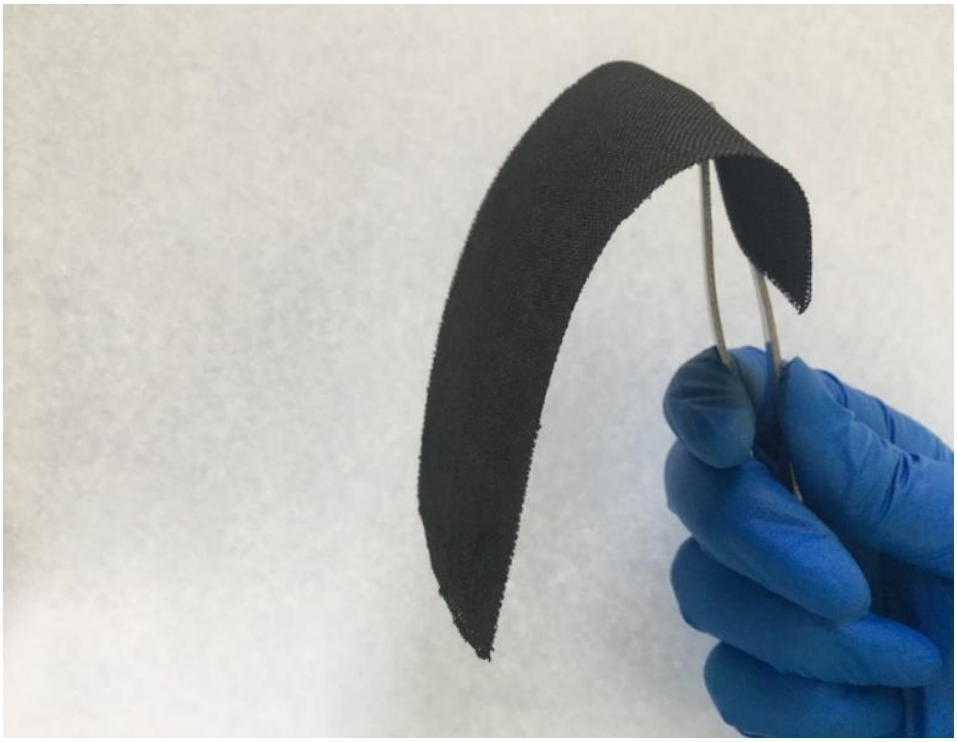

Figure S33. Photograph of bendable carbon cloth after spraying Super P carbon.

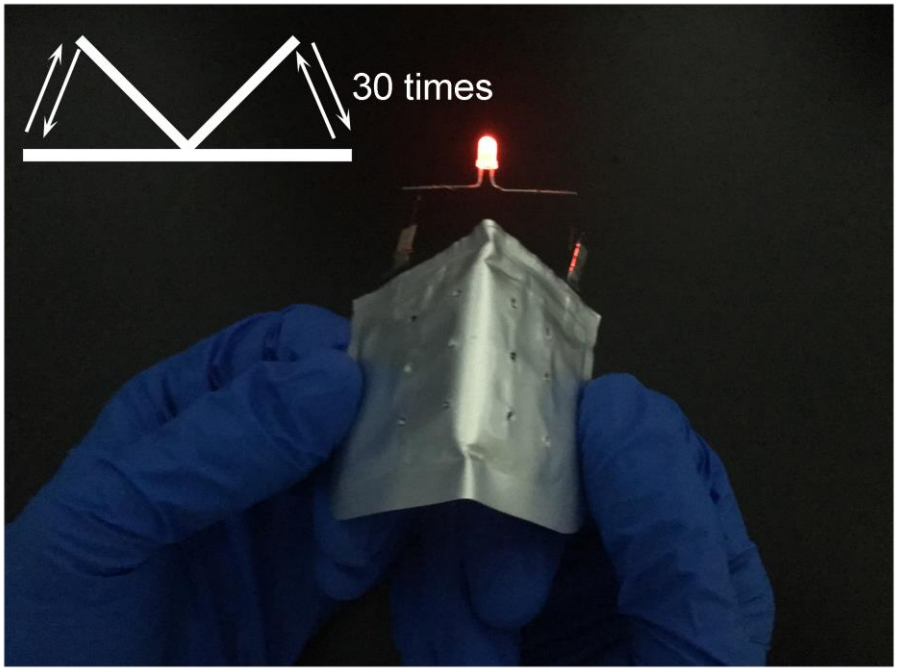

Figure S34. Fatigue test of flexible QPE-based Na–O_2 battery.

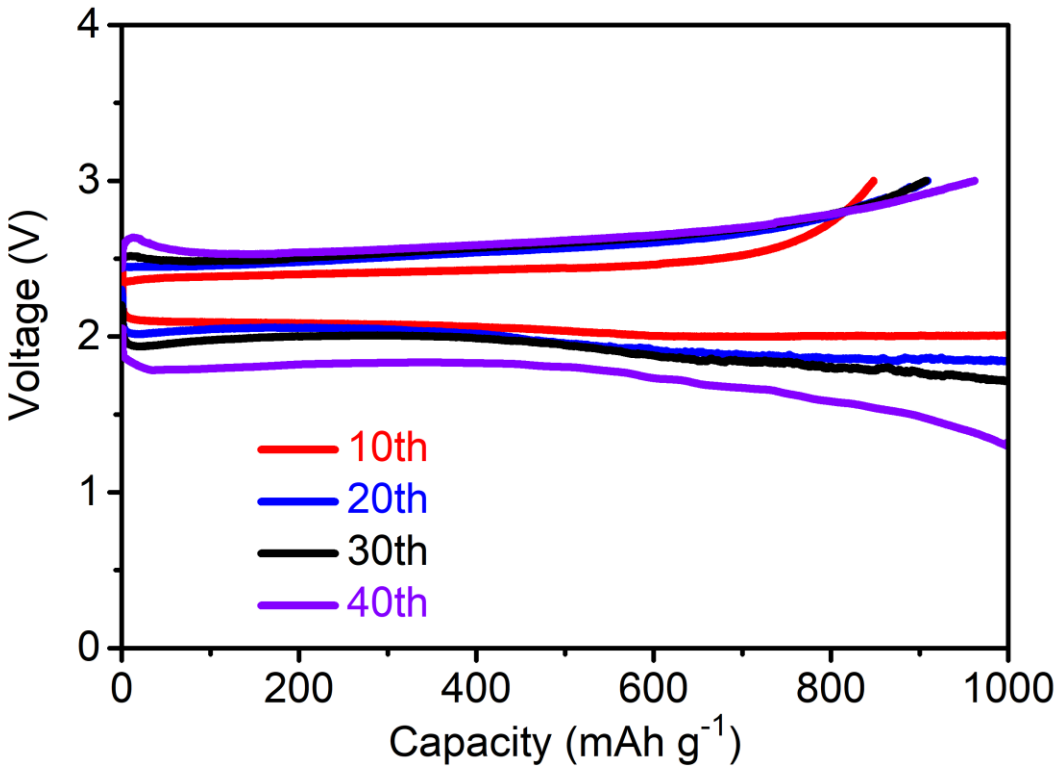

Figure S35. Voltage profiles for flexible QPE-based Na–O_2 battery.

Table S1. Comparison of the electrochemical performance between liquid-based Na–O_2 batteries in recent works and our work.

State	Cathode	Charge terminal voltage	Coulombic efficiency	Capacity&Cycle performance	Flexibility	Refs
Liquid electrolyte	Carbon paper	3.0 V	~90%	0.1 mAh/cm^2, 0.1 mA/cm^2, 60 cycles	No	8
Liquid electrolyte	Co_3O_4@carbon textiles	~3.9 V	100%	500 mAh/g, 100 mA/g, 62 cycles	No	9
Liquid electrolyte	CNT@Co_3O_4	4.5 V	90-100%	300 mAh/g, 300 mA/g, 21 cycles	No	10
Liquid electrolyte	CoB/CNTs	~3.7 V	100%	2000 mAh/g, 100 mA/g 74 cycles	No	11
Liquid electrolyte	Pd/ZnO/C	~2.9 V	100%	0.15 mAh/cm^2, 9 cycles	No	12
Liquid electrolyte	Carbon paper	4.4 V	100%	1000 mAh/g, 500 mA/g, 50 cycles	No	13
Liquid electrolyte	CNTs	—	—	1000 mAh/g, 100 mA/g, 87 cycles	No	14
Liquid electrolyte	NCNT	~4.25 V	100%	300 mAh/g, 300 mA/g, 22 cycles	No	15
Solid-state electrolyte	—	—	—	—	No	16
Quasi-solid state electrolyte	Super P	3.0 V	~97%	1000 mAh/g, 200 mA/g, 80 cycles	Yes	This work

References

(1) Becke, Axel D. Becke's three parameter hybrid method using the LYP correlation functional. *J. Chem. Phys.* **1993**, *98*, 5648-5652.

(2) Lee, C.; ang, W. Parr RG Development of the Colle-Salvetti Correlation-Energy Formula into a Functional of the Electron Density. *Phys. Rev. B: Condens. Matter Mater. Phys.* **1988**, *37*, 785-789.

(3) Vosko, Seymour H.; Wilk, L.; Nusair, M. Accurate spin-dependent electron liquid correlation energies for local spin density calculations: a critical analysis. *Can. J. Phys.* **1980**, *58*, 1200-1211.

(4) Hehre, W. J.; Ditchfield, R.; Pople, J. A. Self-consistent molecular orbital methods. XII. Further extensions of Gaussian-type basis sets for use in molecular orbital studies of organic molecules. *J. Chem. Phys.* **1972**, *56*, 2257-2261.

(5) Clark, T.; Chandrasekhar, J.; Spitznagel, G. W.; Schleyer, P. V. R. Efficient diffuse function-augmented basis sets for anion calculations. III. The 3- 21+G basis set for first- row elements, Li–F. *J. Comput. Chem.* 1**983**, *4*, 294-301.

(6) Hariharan, Praveen C.; John A. Pople. The influence of polarization functions on molecular orbital hydrogenation energies. *Theor. Chim. Acta* **1973**, *28*, 213-222.

(7) Kuo, L., Moradabadi, A., Huang, H., Hwang, B., Kaghazchi, P. Structure and ionic conductivity of the solid electrolyte interphase layer on tin anodes in Na-ion batteries. *J. Power Sources* **2017**, 341, 107-113.

(8) Lin, X.; Sun, Q.; Yadegari, H.; Yang, X.; Zhao, Y.; Wang, C.; Liang, J.; Koo, A.; Li, R.; Sun, X. On the Cycling Performance of Na- O_2 Cells: Revealing the Impact of the Superoxide Crossover toward the Metallic Na. *Adv. Funct. Mater.* **2018**, *28*, 1801904.

(9) Li, N.; Xu, D.; Bao, D.; Ma, J.; Zhang, X.; A binder-free, flexible cathode for rechargeable Na-O_2 batteries. *Chin. J. Catal.* **2016**, *37*, 1172-1179.

(10) Sun, Q.; Liu, J.; Li, X.; Wang, B.; Yadegari, H.; Lushington, A.; Banis, M. N.; Zhao, Y.; Xiao, W.; Chen, N.; Wang, J.; Sham, T.-K.; Sun, X. Atomic Layer Deposited Non- Noble Metal Oxide Catalyst for Sodium–Air Batteries: Tuning the Morphologies and Compositions of Discharge Product. *Adv. Funct. Mater.* **2017**, *27*, 1606662.

(11) Ma, J.-L.; Li, N.; Zhang, Q.; Zhang, X. B.; Wang, J.; Li, K.; Hao, X.-F.; Yan, J.-M. Synthesis of porous and metallic CoB nanosheets towards a highly efficient electrocatalyst for rechargeable Na–O_2 batteries. *Energy Environ. Sci.* **2018**, *11*, 2833-2838.

(12) Ma, L.; Zhang, D.; Lei, Y.; Yuan, Y.; Wu, T.; Lu, J.; Amine, K. High-Capacity Sodium Peroxide Based Na–O_2 Batteries with Low Charge Overpotential via a Nanostructured Catalytic Cathode. *ACS Energy Lett.* **2018**, *3*, 276-277.

(13) Wu, S.; Qiao, Y.; Jiang, K.; He, Y.; Guo, S.; Zhou, H. Tailoring Sodium Anodes for Stable Sodium-Oxygen Batteries. *Adv. Funct. Mater.* **2018**, *28*, 1706374.

(14) Ma, J.-L.; Yin, Y.-B.; Liu, T.; Zhang, X.-B.; Yan, J.-M.; Jiang, Q. Suppressing Sodium Dendrites by Multifunctional Polyvinylidene Fluoride (PVDF) Interlayers with Nonthrough Pores and High Flux/Affinity of Sodium Ions toward Long Cycle Life Sodium Oxygen-Batteries. *Adv. Funct. Mater.* **2018**, *28*, 1703931.

(15) Sun, Q.; Liu, J.; Xiao, B.; Wang, B.; Banis, M.; Yadegari, H.; Adair, K. R.; Li, R.; Sun, X. Visualizing the Oxidation Mechanism and Morphological Evolution of the Cubic- Shaped Superoxide Discharge Product in Na–Air Batteries. *Adv. Funct. Mater.* **2019**, *29*, 1808332.

(16) Faktorovich-Simon, E.; Natan, A.; Peled, E.; Golodnitsky, D. Oxygen redox processes in PEGDME-based electrolytes for Na-air battery. *J. Solid State Electrochem.* **2018**, *22*, 1015–1022.